Discover Chemistry

RESEARCH Open Access

Development of silanized nano-biochar from palm kernel shell for enhanced thermal insulation in polyethylene composites

David Abutu[1*], Barima Money[2], Amani Haruna David[1], A. O. Ameh[1] and Peter Ujulu[3]

*Correspondence:
David Abutu
davidabutu@fuwukari.edu.ng
[1]Department of Chemical Engineering, Federal University Wukari, Wukari, Taraba State, Nigeria
[2]Faculty of Chemical and Process Engineering TechnologyLebuhraya Persiaran Tun Khalil Yaakob, Universiti Malaysia Pahang Al-Sultan Abdullah, KuantanPahang 26300, Malaysia
[3]Department of Central Laboratory, Federal University Wukari, Wukari, Taraba State, Nigeria

Abstract

This study presents the synthesis, characterization, and application of silanized nano-biochar (SNB) derived from palm kernel shell for the development of high-performance low-density polyethylene (LDPE) composites with enhanced thermal insulation and flame retardancy. Nano-biochar was produced via ball milling of pyrolyzed biomass and surface functionalized using 3-aminopropyltriethoxysilane (APTES) at varying concentrations (1–5% v/v). FTIR analysis confirmed that 2% APTES yielded the most effective silanization, as evidenced by the distinct appearance of Si-O-Si, Si-O-C, and N-H functional peaks, along with a reduction in hydroxyl groups. SNB was then incorporated into LDPE at loadings of 1, 3, 5, and 10 wt% to evaluate its effect on thermal, structural, and mechanical properties. The 5 wt% SNB/LDPE composite exhibited optimal multifunctional performance, achieving a 25% reduction in thermal conductivity, improved thermal diffusivity and heat capacity, and enhanced tensile strength and modulus. XRD and DSC analyses revealed a minor reduction in crystallinity and thermal transitions, indicating good matrix compatibility. Flame retardancy was further improved by integrating 10 wt% of commercial flame retardants; ammonium polyphosphate (APP), aluminum hydroxide, and magnesium hydroxide into the optimized composite. The SNB/APP system showed superior performance with a limiting oxygen index (LOI) of 32.5%, UL-94 V-0 rating, and 51% Peak heat release rate (PHRR) reduction. These results demonstrate a synergistic effect between SNB and APP, attributed to intumescent char formation and thermal barrier reinforcement. This study highlights the potential of silanized nano-biochar as a sustainable, multifunctional additive for thermoplastic composites in advanced thermal and fire-protection applications.

Keywords Silanized nano-biochar, Palm kernel shell, Polyethylene composites, Thermal insulation, Flame retardancy

1 Introduction

The growing demand for sustainable, thermally resilient, and fire-safe polymeric materials has catalyzed research in the development of bio-based composites [1–3], particularly those reinforced with carbon-rich fillers such as biochar. LDPE, while valued for

© The Author(s) 2026. **Open Access** This article is licensed under a Creative Commons Attribution-NonCommercial-NoDerivatives 4.0 International License, which permits any non-commercial use, sharing, distribution and reproduction in any medium or format, as long as you give appropriate credit to the original author(s) and the source, provide a link to the Creative Commons licence, and indicate if you modified the licensed material. You do not have permission under this licence to share adapted material derived from this article or parts of it. The images or other third party material in this article are included in the article's Creative Commons licence, unless indicated otherwise in a credit line to the material. If material is not included in the article's Creative Commons licence and your intended use is not permitted by statutory regulation or exceeds the permitted use, you will need to obtain permission directly from the copyright holder. To view a copy of this licence, visit http://creativecommons.org/licenses/by-nc-nd/4.0/.

its mechanical flexibility and cost-effectiveness, suffers from high flammability and poor thermal insulation traits that limit its use in safety critical applications [4–6]. To address these limitations, recent studies have explored the incorporation of biochar, a pyrolyzed biomass derivative, into polyethylene matrices to improve mechanical and flame-retardant performance in an environmentally friendly manner [7, 8]. This creates a clear need for multifunctional fillers that can simultaneously enhance thermal insulation, mechanical integrity, and fire resistance in LDPE composites.

Biochar has been shown to reduce the thermal conductivity of polyolefins by forming tortuous pathways that impede phonon transport, while simultaneously enhancing thermal stability and char yield during combustion [9]. However, conventional biochar particles often exhibit hydrophilicity and poor dispersion in nonpolar matrices such as LDPE, leading to poor filler-matrix interfacial bonding and inconsistent performance. Surface modification techniques particularly silanization using organosilanes such as APTES have been employed to mitigate these issues by grafting functional groups onto the biochar surface [10]. This improves compatibility and allows for more effective stress transfer and thermal resistance in polymer systems [11, 12]. However, most studies focus on untreated or microscale biochar, and there remains a gap in understanding how nanoscale, surface-functionalized biochar can influence composite performance.

Furthermore, nanoscale biochar particles offer a high surface area-to-volume ratio, increasing the potential for interfacial interaction and enhancing the effectiveness of thermal and flame-retardant additives [13–15]. While some studies have evaluated biochar in high-density polyethylene (HDPE) and polypropylene (PP) systems, limited research has addressed the combined effect of SNB and traditional flame retardants like APP, magnesium hydroxide, and aluminum hydroxide on LDPE matrices. Previous studies have largely focused on untreated or microscale biochar, with minimal attention given to silane-functionalized nano-biochar and its role in modifying interfacial chemistry and thermal transport behavior in LDPE. Moreover, the influence of silanization degree on dispersion quality, crystallinity evolution, and multifunctional performance has not been systematically examined. Such synergistic systems can promote intumescent char formation, reduce PHRR, and achieve UL-94 V-0 ratings at relatively low filler loadings [16, 17]. However, the specific mechanisms governing the interaction between silanized nano-biochar and intumescent flame-retardant systems in LDPE remain insufficiently understood, particularly regarding thermal insulation enhancement alongside fire performance. Therefore, this study explicitly addresses this knowledge gap by investigating the optimized silanization of nano-biochar and its synergistic integration with commercial flame retardants in LDPE composites.

This research aims to synthesize and characterize SNB derived from palm kernel shell via pyrolysis and APTES functionalization and to evaluate its role in enhancing the thermal insulation and flame retardancy of LDPE composites. Specifically, we investigate how varying SNB loadings (1–10 wt%) affect thermal, structural, and mechanical properties, and we further examine synergistic effects when the optimal SNB formulation is combined with conventional flame retardants. This work advances the field by offering a scalable, bio-based strategy for producing multifunctional LDPE composites, contributing to both material circularity and fire safety in polymer applications.

2 Experimental

2.1 Raw material preparation

Palm kernel shells (PKS) were collected from GAV Gambang palm oil processing facility in Pahang Malaysia. The PKS was manually sorted to remove contaminants such as fibrous residues, stones, and organic matter. After visual inspection, the shells were washed thoroughly with tap water, followed by rinsing with deionized water to eliminate surface impurities. The cleaned shells were spread in a single layer and oven-dried at 105 °C for 24 h to reduce their moisture content to below 5%, a critical step to ensure consistency in thermal decomposition during pyrolysis.

Following drying, the PKS were subjected to pyrolysis to convert them into biochar. Pyrolysis was performed in a horizontal tubular furnace (Carbolite Gero STF series) under a nitrogen atmosphere (flow rate: 100 mL/min) to create an oxygen-free environment, which minimizes combustion and enhances carbon retention. The temperature was ramped from ambient to 500 °C at a rate of 10 °C/min and held isothermally for 2 h. The resulting biochar was allowed to cool to room temperature under nitrogen to prevent oxidation and then ground using a mortar and pestle to obtain a coarse powder for further size reduction [18, 19].

2.2 Nano-biochar synthesis via ball milling

The coarse biochar powder was converted into nanoscale particles using a planetary ball mill (Retsch PM100) equipped with a zirconia jar and milling balls. Approximately 100 g of the ground biochar was placed in a 1000 mL jar with zirconia balls at a ball-to-powder weight ratio of 10:1. The milling process was conducted at a rotational speed of 400 rpm for a total duration of 6 h, with 15 min rest intervals after every 30 min of milling to prevent overheating and preserve structural properties. This mechanical approach to particle size reduction enhances the surface area and reactivity of biochar, critical for maximizing interfacial interactions in polymer composites [20].

Post-milling, the nano-biochar was collected and sieved through a 200-mesh screen to ensure uniformity in particle size (< 75 μm). To remove any metallic contaminants introduced during the milling process, the powder was subjected to magnetic separation and then washed thoroughly with ethanol followed by distilled water. Finally, the nano-biochar was oven-dried at 80 °C for 12 h and stored in desiccators until further use [21, 22].

2.3 Surface silanization of nano-biochar

To enhance compatibility with the polyethylene matrix and improve filler dispersion, the surface of nano-biochar was chemically modified via silanization using APTES. 50.0 g of nano-biochar was dispersed in 500 mL of absolute ethanol in a 250 mL round-bottom flask and subjected to ultrasonication for 30 min to ensure homogeneous dispersion. Then, 1–5% v/v APTES was added dropwise under magnetic stirring, followed by the addition of 50 mL of deionized water to facilitate hydrolysis of the silane groups. The reaction mixture was refluxed at 80 °C for 4 h to promote condensation reactions between the hydrolyzed silane and surface hydroxyl groups on the biochar. After the reaction, the modified nano-biochar was filtered using Whatman No. 1 filter paper and washed three times with ethanol to remove unreacted silane. The solid was then dried under vacuum at 80 °C for 12 h and thereafter characterized using FTIR [23, 24].

2.4 Composite fabrication via melt blending

The silanized nano-biochar was incorporated into a LDPE matrix via melt blending using a laboratory-scale co-rotating twin-screw extruder (Thermo Scientific HAAKE MiniLab II). Prior to compounding, LDPE pellets and biochar were dried separately at 80 °C for 6 h to eliminate moisture. Blending was performed at a barrel temperature of 170 °C, a screw speed of 100 rpm, and a residence time of 8 min. SNB loading levels of 1, 3, 5, and 10 wt% were investigated to assess the effect of filler content on composite properties.

The extrudate was immediately quenched in a cold-water bath and pelletized. The pellets were then compressed into beads of 2 mm thickness using a hot press (Carver 3851) at 170 °C and 5 MPa for 10 min, followed by cold pressing to room temperature [25, 26]. The use of melt blending ensures uniform dispersion of filler particles and mimics scalable industrial polymer processing. Careful control of temperature and shear conditions minimized polymer degradation and maintained biochar integrity. The resulting beads were used for all characterized [27, 28].

2.5 Characterization techniques

2.5.1 Fourier transform infrared spectroscopy (FTIR)

FTIR analysis was conducted to confirm the successful surface functionalization of nano-biochar with APTES and to identify the presence of characteristic functional groups. Spectra were recorded using a Bruker Tensor 27 spectrometer over the wavenumber range of 4000–500 cm^{-1} at a resolution of 4 cm^{-1}. Each spectrum was collected by averaging 32 scans to improve signal-to-noise ratio and ensure spectral reproducibility. Samples were prepared using the attenuated total reflectance (ATR) mode to minimize additional sample preparation steps. Background correction was performed prior to each measurement. The obtained spectra were analyzed to identify key vibrational bands corresponding to Si–O–Si, Si–O–C, N–H, and hydroxyl groups. Peak assignments were made based on standard reference databases and literature values to verify the extent of silanization.

2.5.2 Scanning electron microscopy (SEM/FESEM)

Surface morphology, particle size distribution, and dispersion behavior of nano-biochar within the LDPE matrix were examined using scanning electron microscopy (SEM, JEOL JSM-7600 F). Prior to imaging, samples were sputter-coated with a thin gold layer using a Quorum Q150T coater to minimize surface charging and improve image clarity. High-resolution field emission SEM (FESEM) imaging was conducted to further assess nanoscale structural features, agglomeration behavior, and filler–matrix interfacial interactions. Micrographs were obtained at multiple magnifications to ensure representative analysis. Particle size measurements were performed using ImageJ software based on several randomly selected regions to obtain statistically reliable average values [29].

2.5.3 X-ray diffraction (XRD)

XRD analysis was performed using a PANalytical X'Pert PRO diffractometer equipped with Cu Kα radiation (λ = 1.5406 Å), operated at 40 kV and 30 mA. Diffraction patterns were recorded over a 2θ range of 5°–80° at a scanning rate of 2°/min to evaluate the crystalline structure of LDPE and its composites. The degree of crystallinity was determined

by deconvoluting crystalline and amorphous peaks using peak fitting and integration methods. The crystallinity index was calculated from the ratio of crystalline peak area to the total diffracted area. Baseline correction and smoothing were performed using OriginPro software to improve peak resolution and accuracy.

2.5.4 Thermogravimetric analysis (TGA)

Thermogravimetric analysis was carried out using a TA Instruments Q500 analyzer to evaluate thermal stability and degradation behavior. Approximately 10 mg of each sample was placed in a platinum pan and heated from 30 to 800 °C under a nitrogen atmosphere to prevent oxidative degradation. The heating rate was maintained at 10 °C/min to ensure uniform thermal exposure. Key parameters including onset degradation temperature (T_{onset}), temperature at maximum weight loss (T_{max}), and residual char yield at 800 °C were extracted from the thermograms. These values were used to assess the thermal resistance and char-forming ability of the composites [30, 31].

2.5.5 Differential scanning calorimetry (DSC)

DSC measurements were performed using a TA Instruments Q2000 calorimeter to determine thermal transition behavior. Samples weighing approximately 5–8 mg were sealed in aluminum pans and subjected to heating from – 50 to 200 °C at a rate of 10 °C/min under nitrogen atmosphere. The melting temperature (T_m), glass transition temperature (Tg), and specific heat capacity (Cp) were determined from the thermograms. The degree of crystallinity was calculated from the melting enthalpy relative to that of 100% crystalline polyethylene. All measurements were conducted in triplicate to ensure reproducibility [32, 33].

2.5.6 Thermal diffusivity and thermal conductivity

Thermal diffusivity (α) was measured using a Netzsch LFA 447 laser flash analyzer in accordance with ASTM E1461. Disk-shaped specimens were prepared with uniform thickness and coated with a thin graphite layer to enhance laser energy absorption and emissivity. The thermal diffusivity was calculated from the sample thickness (L) and half-rise time ($t_1/_2$) using Eq. (1). Thermal conductivity (k) was subsequently calculated using Eq. (2), incorporating measured density and specific heat capacity values. Multiple measurements were performed for each formulation to ensure statistical reliability.

2.5.7 Mechanical testing

Mechanical properties were evaluated using a universal testing machine (Instron 3365) following ASTM D638 standards. Dumbbell-shaped specimens were die-cut from compression-molded sheets with uniform thickness and tested at a crosshead speed of 50 mm/min under ambient conditions. Tensile strength (σ) was calculated using Eq. (3), while Young's modulus (E) was derived from the slope of the initial linear region of the stress–strain curve using Eq. (4). For each formulation, five specimens were tested and the average values along with standard deviations were reported to ensure statistical significance [34–36].

2.5.8 Flame retardancy testing

The UL-94 vertical burning test was conducted according to ASTM D3801 to evaluate flammability behavior. Samples were vertically mounted and exposed to a standardized methane flame for 10 s, followed by removal of the flame and re-application for an additional 10 s [15]. After-flame time, afterglow time, melting behavior, and dripping characteristics were recorded to determine the UL-94 rating (V-0, V-1, or V-2). The limiting oxygen index (LOI) was measured according to ASTM D2863 using a controlled oxygen–nitrogen mixture, and values were calculated using Eq. (5). Peak heat release rate (PHRR) was determined using a micro-scale combustion calorimeter (ASTM D7309), which measures heat release during controlled pyrolysis and combustion. Time to Ignition (TTI) was evaluated using a cone calorimeter in accordance with ISO 5660 under an external heat flux of 35 kW/m², providing a quantitative measure of ignition resistance.

$$\alpha = \frac{0.1388\, L^2}{t_{1/2}} \tag{1}$$

$$k = \alpha \cdot \rho \cdot Cp \tag{2}$$

$$\sigma = \frac{F_{max}}{A_o} \tag{3}$$

$$E = \frac{\Delta_\sigma}{\Delta_\in} \tag{4}$$

$$LOI\ (\%) = \frac{[O_2]}{[O_2] + [N_2]} \times 100 \tag{5}$$

3 Results and discussion

3.1 Preparation and characterization of NB and SNB

The raw PKS was successfully pyrolyzed at 600 °C under a nitrogen atmosphere, yielding a carbon-rich biochar. Subsequent ball milling for 6 h produced nano-biochar particles averaging 46.3 nm in diameter, confirmed by FESEM as shown in Fig. 1. The reported average particle diameter represents the size of primary nano-biochar particles measured from multiple representative regions. The larger features observed in certain areas of the SEM image correspond to agglomerated clusters formed during drying and sample preparation and were therefore excluded from primary particle size analysis. This nanoscale dimension ensured better surface area exposure and polymer interaction. BET analysis showed a specific surface area of 635 m²/g, which is 30% higher than the 480–500 m²/g range reported by [37, 38] for similar agricultural waste-derived biochars. High surface areas in biochars produced at ~600 °C have been widely reported and are attributed to the development of microporous carbon frameworks during devolatilization and aromatization of lignocellulosic biomass. The increased surface area provides a greater density of oxygen-containing functional groups, which are essential anchoring sites for silane coupling reactions [39, 40]. For the silanization process, conducted with APTES, Fig. 2 presents the FTIR spectra of unmodified NB and samples silanized with varying concentrations (1–5% v/v) of APTES. Prior to analysis, all spectra were baseline-corrected, and peak assignments were carried out by comparison with characteristic vibrational band ranges reported in the literature for lignocellulosic biochar and silane

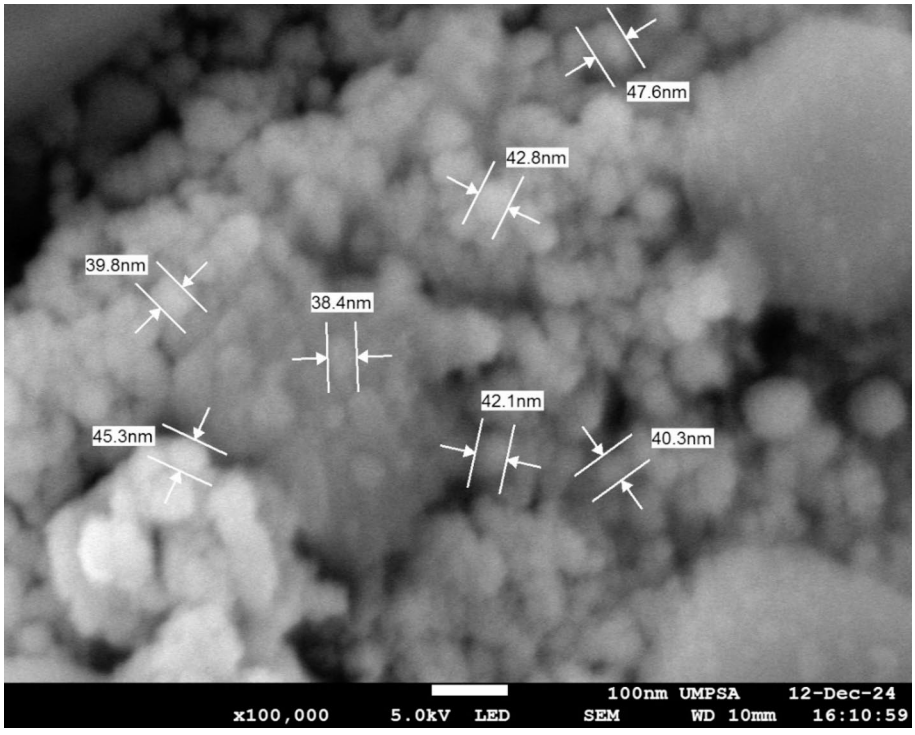

Fig. 1 FESEM of the synthesized nanobiochar

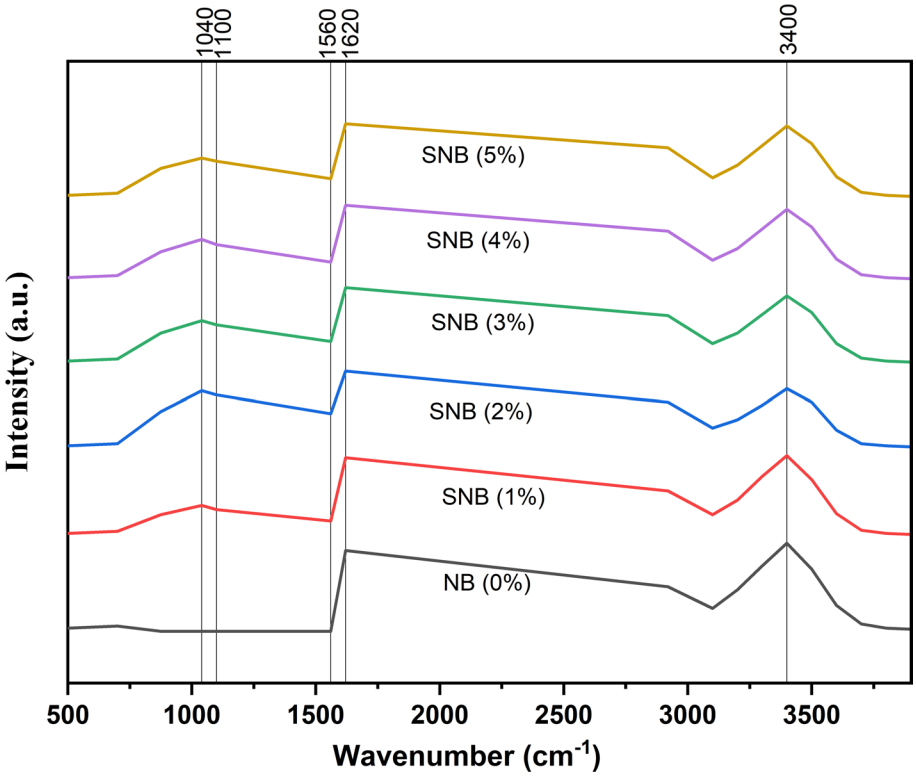

Fig. 2 FTIR spectra of unmodified Nano-biochar (NB) and modified NB

coupling agents. The NB spectrum exhibits characteristic features of lignocellulosic biochar, including a broad O–H stretching band around 3400 cm^{-1} due to surface hydroxyl groups and adsorbed moisture, and a sharp band near 1620 cm^{-1} attributed to C = C stretching vibrations from aromatic structures [41].

Upon silanization, distinct silane-related bands progressively emerge, particularly in the 2% APTES spectrum. Notably, peaks at 1560 cm^{-1} (N–H bending), 1100 cm^{-1} (Si–O–C stretching), and 1040 cm^{-1} (Si–O–Si symmetric stretching) become more prominent, indicating successful grafting of silane molecules onto the nano-biochar surface [42, 43]. The band at ~ 1560 cm^{-1} is consistent with N–H bending vibrations from amine groups of APTES, confirming the presence of organosilane moieties [44]. Additionally, the bands in the region of 1000–1100 cm^{-1} correspond to overlapping Si–O–C and Si–O–Si stretching vibrations, which are characteristic of covalent bonding with hydroxylated surfaces and siloxane network formation [45–47]. Simultaneously, the intensity of the O–H band diminishes significantly at 2% APTES, suggesting effective reaction between the silanol groups of APTES and the hydroxylated surface of the biochar [44]. This observation is consistent with the established silanization mechanism involving hydrolysis of alkoxysilane groups followed by condensation with surface –OH groups to form Si–O–C linkages [44]. Beyond the 2% concentration, the silane-associated peaks exhibit little to no further increase in intensity, and in some cases, such as at 3–5% APTES, they slightly decrease, indicating possible steric hindrance, silane self-condensation, or saturation of reactive surface sites [40]. The relatively weak or plateauing peak intensities at these higher concentrations suggest less efficient grafting or potential formation of silane aggregates rather than uniform surface bonding. In contrast, the 1% APTES spectrum shows only faint silane peaks, implying insufficient coverage [48]. It is also noted that some absorption bands appear broad due to the heterogeneous and amorphous nature of biochar, which can result in overlapping vibrational modes and reduced spectral resolution. Nevertheless, the consistent emergence of characteristic silane-related peaks across the modified samples supports the reliability of the chemical modification. Collectively, these observations support the conclusion that 2% APTES provides the most effective and controlled surface functionalization of palm kernel shell-derived nano-biochar. This optimal modification enhances compatibility with polymer matrices and is expected to improve filler dispersion and interfacial bonding in the resulting composites. Table 1 presents a comparative summary of the properties of the NB and SNB synthesized.

The XRD spectra As shown in Fig. 3 shows characteristic crystalline peaks at approximately 21.5° and 23.8° 2θ, which correspond to the (110) and (200) planes of the orthorhombic polyethylene crystal structure. These peaks are retained across all formulations, indicating that the addition of SNB does not fundamentally disrupt the crystalline phase of LDPE. However, a gradual decrease in peak intensity and sharpness is observed with

Table 1 Physicochemical properties of raw biochar and SNB (Mean ± SD, $n = 5$)

Property	Raw biochar	SNB (2% APTES)
Average particle size (nm)	46.3 ± 2.1	86.5 ± 3.4
FTIR key peaks	–OH, C = C	Si–O–Si, Si–O–C, N–H
T_{onset} (°C)	317 ± 2	359 ± 3
T_{max} (°C)	432 ± 3	470 ± 2
Residual char at 800 °C (%)	28.4 ± 0.8	39.2 ± 1.0
BET surface area (m^2/g)	635 ± 12	300 ± 10

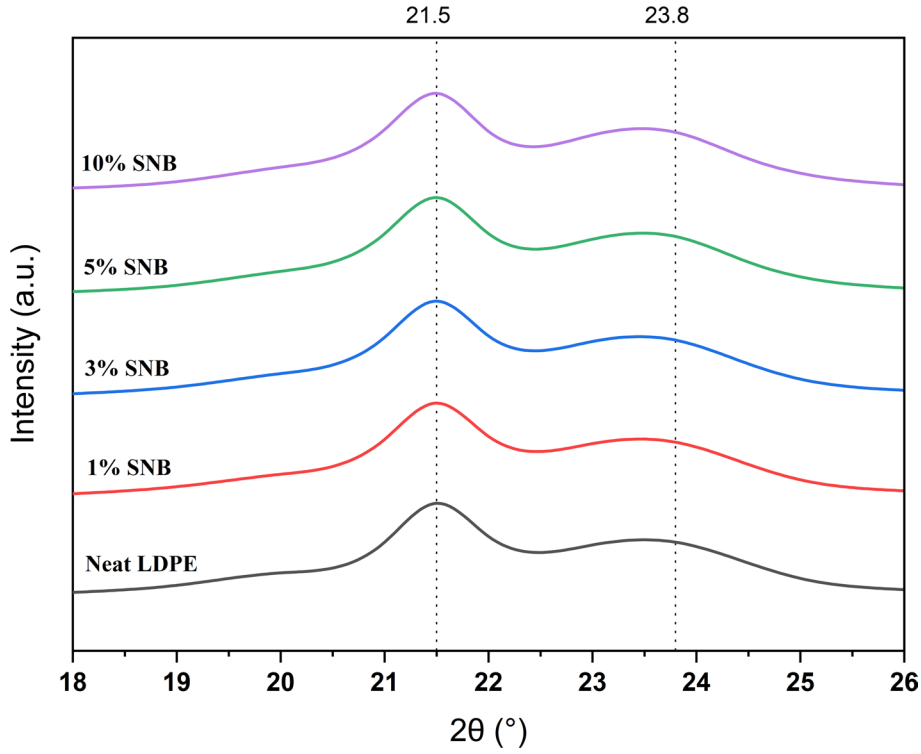

Fig. 3 XRD profiles of unmodified LDPE and LDPE composites reinforced with 1, 3, 5, and 10 wt% SNB

increasing SNB content, particularly at 10 wt%, suggesting a modest reduction in crystalline order. This trend is confirmed by the crystallinity index, which decreases from 72.0% for neat LDPE to 67.2% at 10 wt% SNB.

This reduction in crystallinity is attributed to the presence of SNB particles disrupting the regular packing of LDPE chains, especially when the filler is uniformly dispersed at the nanoscale. The silanized surface of the biochar improves interfacial compatibility but also introduces localized regions of steric interference that limit chain folding and crystal growth. These findings align with previous work by Zhang et al. [7], who observed similar crystallinity suppression in HDPE composites reinforced with biochar fillers. Overall, the XRD analysis confirms that SNB incorporation slightly reduces the degree of crystallinity in LDPE but does not induce amorphization, preserving the semi-crystalline structure required for mechanical integrity.

TGA curve as shown in Fig. 4 for the neat LDPE and its composites containing 1–10 wt% SNB under nitrogen atmosphere shows a single-step degradation process starting at approximately 312 °C for the Neat LDPE, with complete breakdown by approximately 500 °C. In contrast, SNB-reinforced composites demonstrate a clear improvement in thermal stability, with the onset of degradation (T_{onset}) shifting upward to 351 °C for the 5 wt% SNB sample and residual char content increasing significantly to 22.2% at 10 wt%. These enhancements can be attributed to the thermal barrier effect and high thermal stability of biochar, which slows heat and mass transfer during decomposition [49, 50].

Moreover, the increased char residue is indicative of the carbonaceous framework introduced by SNB, which promotes the formation of a stable protective layer during thermal degradation. This behavior is consistent with prior findings on biochar-reinforced polyolefins, where char formation was found to be critical for both flame

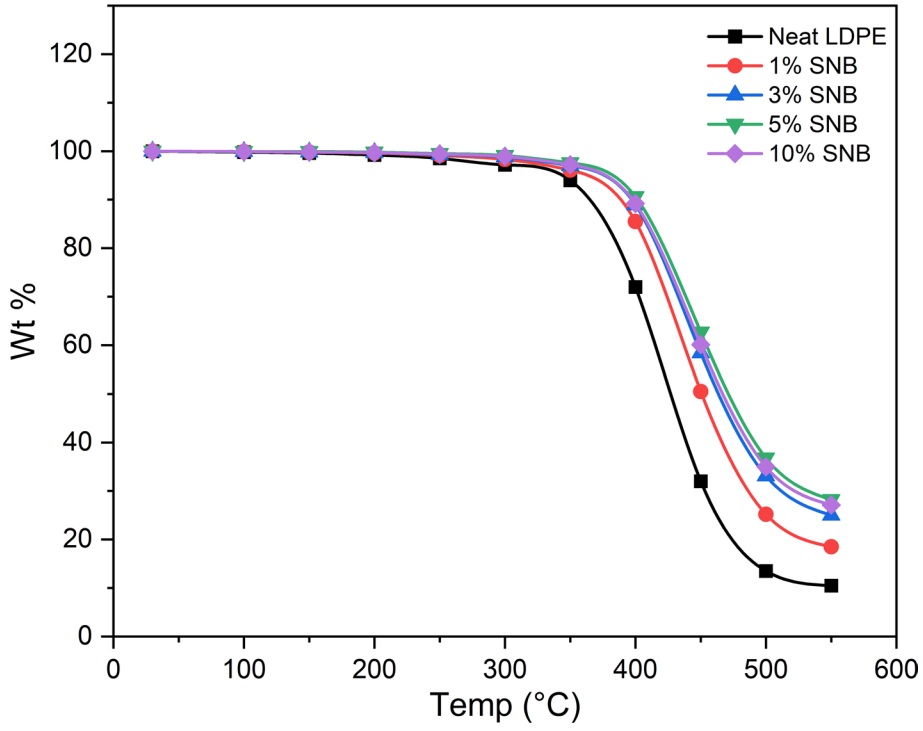

Fig. 4 displays the TGA curves of neat LDPE and its composites containing 1–10 wt% SNB under nitrogen atmosphere

Table 2 Thermal Transitions and Conductivity Properties of SNB/LDPE Composites (2% APTES SNB) (Mean ± SD, $n = 5$)

SNB content (wt%)	Melting temperature, T_m (°C)	Glass transition temperature, T_g (°C)	Thermal conductivity (W/m·K)	Thermal diffusivity (mm^2/s)	Specific heat capacity (J/g·K)	Density (g/cm^3)
0 (neat PE)	112.5 ± 0.3	−109.2 ± 0.4	0.245 ± 0.006	0.165 ± 0.004	1.72 ± 0.03	0.918 ± 0.002
1	112.3 ± 0.2	−109.0 ± 0.3	0.228 ± 0.005	0.172 ± 0.005	1.78 ± 0.04	0.924 ± 0.003
3	112.0 ± 0.3	−108.8 ± 0.2	0.210 ± 0.004	0.185 ± 0.006	1.83 ± 0.03	0.931 ± 0.002
5	111.7 ± 0.4	−108.4 ± 0.3	0.185 ± 0.003	0.198 ± 0.004	1.88 ± 0.02	0.936 ± 0.002
10	111.5 ± 0.5	−108.2 ± 0.4	0.182 ± 0.004	0.207 ± 0.005	1.93 ± 0.04	0.948 ± 0.003

retardancy and thermal resistance [9, 51]. While the 10 wt% SNB sample showed slightly lower T_{onset} and T_{max} compared to 5 wt%, this may be due to filler agglomeration reducing dispersion uniformity. Overall, the TGA results confirm that SNB is an effective thermal stabilizer for LDPE, with optimal performance observed around 5 wt% loading.

3.2 Thermal properties SNB/LDPE composites (2% APTES SNB)

As shown in Table 2, increasing the loading of 2% SNB in the LDPE matrix gradually affects the thermal transition behavior and conductivity performance. A slight reduction in both melting temperature (T_m) and glass transition temperature (T_g) was observed, indicating that SNB mildly disrupts the crystalline and amorphous regions of the polymer matrix [52]. This is consistent with the XRD results showing decreased crystallinity. Thermal conductivity decreased from 0.245 W/m·K in neat LDPE to 0.182 W/m·K at 10 wt% SNB, with the most notable drop occurring between 0 and 5 wt%, confirming SNB's effectiveness in interrupting heat transfer pathways [53, 54]. In contrast, both thermal

diffusivity and specific heat capacity increased with SNB content, peaking at 1.93 J/g·K and 0.207 mm^2/s, respectively, which suggests improved thermal inertia and slower heat propagation beneficial for insulation applications [55]. These changes are attributed to the formation of a thermally resistant SNB network and increased interfacial phonon scattering, further enhanced by the improved matrix-filler adhesion due to silanization.

Furthermore, the incorporation of SNB into LDPE improved the mechanical performance up to a critical threshold [56]. Tensile strength and Young's Modulus increased steadily from 12.8 MPa and 210 MPa in neat LDPE to 14.3 MPa and 248 MPa at 5 wt% SNB, respectively as shown in Table 3. This enhancement can be attributed to better load transfer through the polymer-filler interface due to strong interfacial bonding from the silane-treated biochar. However, at 10 wt%, both properties declined slightly, suggesting the onset of filler agglomeration and micro-defect formation. Meanwhile, elongation at break showed a consistent decline with increasing SNB, indicating reduced ductility, which is typical of filler-reinforced systems. The results confirm that an optimal SNB loading of around 5 wt% provides a good balance between stiffness, strength, and processability without severely compromising flexibility, an important consideration in packaging or insulation applications.

3.3 Flame retardancy performance

Based on the thermal and mechanical evaluations of LDPE composites containing 2% APTES-SNB, the formulation with 5 wt% SNB was identified as the optimal composition. At this loading, the composite exhibited the lowest thermal conductivity (0.185 W/m·K), indicating improved insulation efficiency, while simultaneously maintaining the highest tensile strength (14.3 MPa) and Young's modulus (248 MPa), demonstrating mechanical reinforcement without embrittlement [57]. In addition, T_g and T_m remained stable, confirming that polymer crystallinity was not adversely affected, and the specific heat capacity increased to 1.88 J/g·K, suggesting enhanced thermal inertia. Higher SNB loadings led to signs of filler agglomeration and marginal mechanical gains, whereas lower loadings provided less pronounced thermal insulation improvement [58]. Therefore, 5 wt% SNB was selected as the base matrix because it provided the optimal combination of reduced thermal conductivity, enhanced mechanical strength, preserved thermal transitions, and good processability, ensuring structural integrity prior to flame-retardant incorporation. Building on this optimized LDPE/SNB matrix, three commercial flame retardants (APP, $Al(OH)_3$, $Mg(OH)_2$) were incorporated at 10 wt% to specifically evaluate their synergistic effects on fire resistance. Based on the established thermal and mechanical performance of the optimized 5 wt% SNB composite, these additives are expected to maintain the composite's structural and thermal integrity, consistent with literature reports showing that similar flame retardants do not significantly degrade LDPE-based composites while improving flame retardancy [59]. Testing was done using

Table 3 Mechanical properties of SNB/LDPE composites (2% APTES SNB) (Mean ± SD, $n = 5$)

SNB content (wt%)	Tensile strength (MPa)	Young's modulus (MPa)	Elongation at break (%)
0 (neat PE)	12.8 ± 0.4	210 ± 5	635 ± 18
1	13.3 ± 0.5	225 ± 6	592 ± 15
3	14.1 ± 0.3	240 ± 4	553 ± 12
5	14.3 ± 0.4	248 ± 7	498 ± 10
10	13.0 ± 0.6	242 ± 6	432 ± 13

10 wt% loadings of three commercial flame retardants: APP, $Al(OH)_3$, $Mg(OH)_2$. Each additive was dry blended with the optimized LDPE/SNB matrix, compounded via twin screw extrusion, and processed under controlled thermal and shear conditions to ensure uniform dispersion prior to fire testing [58]. Flame retardancy was evaluated according to standardized methods, recording multiple parameters including limiting oxygen index (LOI), UL-94 vertical burn rating, peak heat release rate (PHRR), time to ignition (TTI), residual char, melting and dripping behavior, ignition of the underlying cotton, after flame time, and afterglow time.

The flame retardancy results in Table 4 demonstrate that incorporating 5 wt% SNB alone enhances the fire resistance of LDPE, increasing the LOI from 17.2% to 21.8% and reducing PHRR by 30%. However, the most significant improvements were observed when SNB was combined with APP, achieving an average LOI of 32.5%, a UL-94 V-0 rating, and a 51% reduction in PHRR compared to neat LDPE. Observations showed limited melting of the composite, no ignition of the underlying cotton, short after flame times (< 2 s), and negligible afterglow (< 5 s), confirming effective fire barrier formation [60]. This is attributed to synergistic effects: APP promotes intumescent char formation while SNB provides a thermally stable carbon scaffold that supports barrier integrity. These results are in line with recent studies, such as the use of microencapsulated APP and intumescent systems, which reported LOI values above 30% and PHRR reductions of 70% in LDPE composites [61, 62].

While aluminum hydroxide and magnesium hydroxide also enhanced flame retardancy, their performance was slightly lower than that of the SNB/APP system. This is likely due to their primarily endothermic decomposition mechanism, which absorbs heat but produces less protective char. The SNB/$Al(OH)_3$ and SNB/$Mg(OH)_2$ systems achieved LOI values of 27.9% and 26.5% respectively, both meeting V-1 UL-94 standards with moderate PHRR reductions. For these systems, minor melting was observed with occasional dripping, but no ignition of the cotton occurred; after flame and afterglow times were slightly longer (2–6 s), consistent with their endothermic protection mechanism. Tensile strength and Young's modulus were largely preserved across all flame-retardant composites, demonstrating that the incorporation of these additives did not compromise mechanical integrity. Based on controlled processing and previous reports, uniform dispersion of SNB and flame-retardant particles is expected to be maintained, supporting structural stability and efficient barrier formation during combustion [63]. These findings confirm that the optimized flame-retardant LDPE/SNB composites provide enhanced fire resistance while maintaining the thermal, mechanical, and morphological properties of the base composite, offering a sustainable, halogen-free solution for multifunctional applications [60].

3.4 Morphological analysis of neat LDPE and SNB-reinforced composites

Figure 5 presents visual images of the neat LDPE and the LDPE/SNB composite. The neat LDPE sample exhibits a relatively smooth and homogeneous appearance, typical of unfilled thermoplastics. In contrast, the LDPE composite containing SNB appears darker and more matte, indicating uniform dispersion of the carbonaceous filler within the polymer matrix. The visual opacity and color shift result from the high surface area and absorptive nature of the biochar, which enhances the composite's ability to block light and potentially improve thermal shielding. No phase separation or large agglomerates

Table 4 Flame retardancy and material performance of 5 wt% SNB/LDPE composites with different 10 wt% flame retardants (mean ± SD, $n = 5$)

Formulation	Thermal conductivity (W/m·K)	Tensile strength (MPa)	Young's modulus (MPa)	Limiting oxygen index (LOI, %)	UL-94 rating	PHRR, kW/m^2)	Time to ignition (TTI, s)	Residual char at 800 °C (%)
Neat LDPE	0.210 ± 0.02	12.5 ± 0.3	230 ± 5	17.2 ± 0.3	NR	547 ± 9	31 ± 2	9.3 ± 0.5
LDPE + 5% SNB	0.185 ± 0.01	14.3 ± 0.5	248 ± 3	21.8 ± 0.5	V-2	382 ± 7	39 ± 1	22.2 ± 0.6
SNB/LDPE + APP	0.187 ± 0.02	14.0 ± 0.3	245 ± 2	32.5 ± 0.6	V-0	267 ± 6	51 ± 2	31.6 ± 0.8
SNB/LDPE + $Al(OH)_3$	0.188 ± 0.01	13.8 ± 0.2	243 ± 4	27.9 ± 0.4	V-1	312 ± 5	44 ± 1	28.1 ± 0.7
SNB/LDPE + $Mg(OH)_2$	0.189 ± 0.03	13.7 ± 0.2	242 ± 3	26.5 ± 0.5	V-1	336 ± 8	42 ± 2	26.9 ± 0.6

are visually evident, suggesting that the silanization process successfully improved the compatibility and interfacial adhesion between the SNB and LDPE.

Figure 6 provides SEM micrographs comparing the surface morphology of the neat LDPE and the LDPE/SNB composite. The neat LDPE surface is characteristically smooth with minimal surface features, while the composite exhibits a more textured and roughened morphology due to the incorporation of nano-biochar. At higher magnification, the SNB particles are observed to be well dispersed, with minimal clustering or agglomeration, indicating effective particle integration. The interfacial regions appear tightly bound, supporting the hypothesis that silane modification via APTES enhanced the filler–matrix interaction. Such uniform dispersion is critical to achieving improved mechanical reinforcement and thermal performance, as it minimizes stress concentration zones and promotes load transfer across the matrix. These morphological findings corroborate the improvements observed in tensile strength and thermal stability discussed in later sections.

3.5 Comparative analysis of flame retardancy performance

To evaluate the effectiveness of the SNB and APP system developed in this study, a comparative matrix was constructed using data from related literature. Table 5 highlights key flame retardancy performance indicators namely LOI, PHRR, char residue, and UL-94 rating for polymer composites containing various biochar and inorganic flame-retardant systems. From the matrix, it is evident that the system developed in this study surpasses several reported flame-retardant biochar systems in performance. Most notably, a LOI of 32.5% and a UL-94 V-0 rating were achieved at just 10 wt% total additive loading (5% SNB and 2% APP), which is significantly more efficient compared to 40–50 wt% used in other studies. The PHRR was also substantially reduced (51% lower than neat LDPE), demonstrating effective suppression of heat release and improved thermal barrier formation. Additionally, the residual char at 800 °C (31.6%) indicates strong char stability, contributing to sustained flame retardancy during combustion. Although Huang et al. (2020) reported a lower PHRR (323.3 kW/m^2), it required a high talc loading (50%) and did not attain V-0 classification. Similarly, Khan et al. (2023) used 40% biochar to reach a lower LOI (25.3%) and a lesser flame rating (V-1), underscoring the enhanced performance of the SNB/APP system due to synergistic effects like char formation and silane-induced compatibility. This confirms the viability of SNB as a multifunctional, efficient filler for developing thermally resistant polymer composites. This superior performance can be attributed to the synergistic effects of silane-functionalized nano-biochar and APP, including improved interfacial compatibility, enhanced intumescent char formation, and thermal barrier reinforcement, which collectively reduce flammability while maintaining mechanical integrity. These findings confirm the viability of SNB as a multifunctional, efficient filler for developing thermally resistant and flame-retardant polymer composites at significantly lower additive loadings compared to conventional systems.

3.6 Proposed mechanism of SNB functionalization and its role in composite performance

The enhanced thermal, mechanical, and flame-retardant performance of the SNB/LDPE composites can be attributed to the surface modification of nano-biochar via silanization and the synergistic interactions with flame retardants, particularly APP. The functionalization process begins with the hydrolysis of APTES in the presence of water and

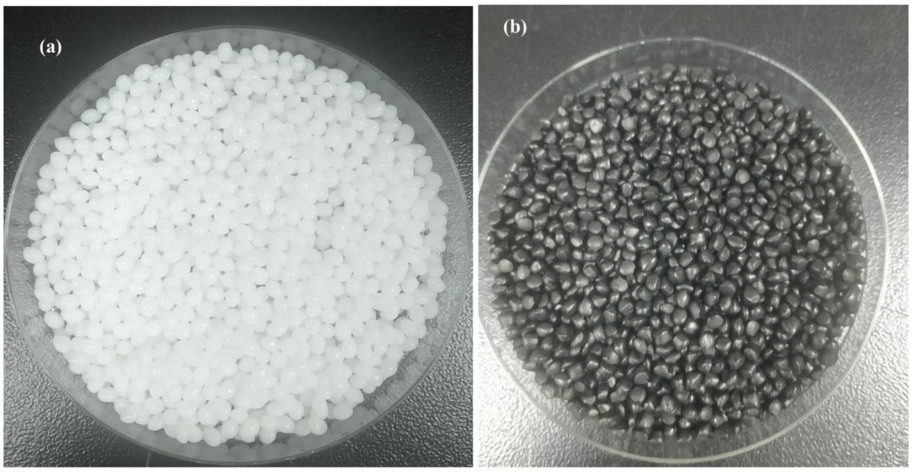

Fig. 5 Image of neat LDPE (**a**), synthesized SNB/LDPE (**b**)

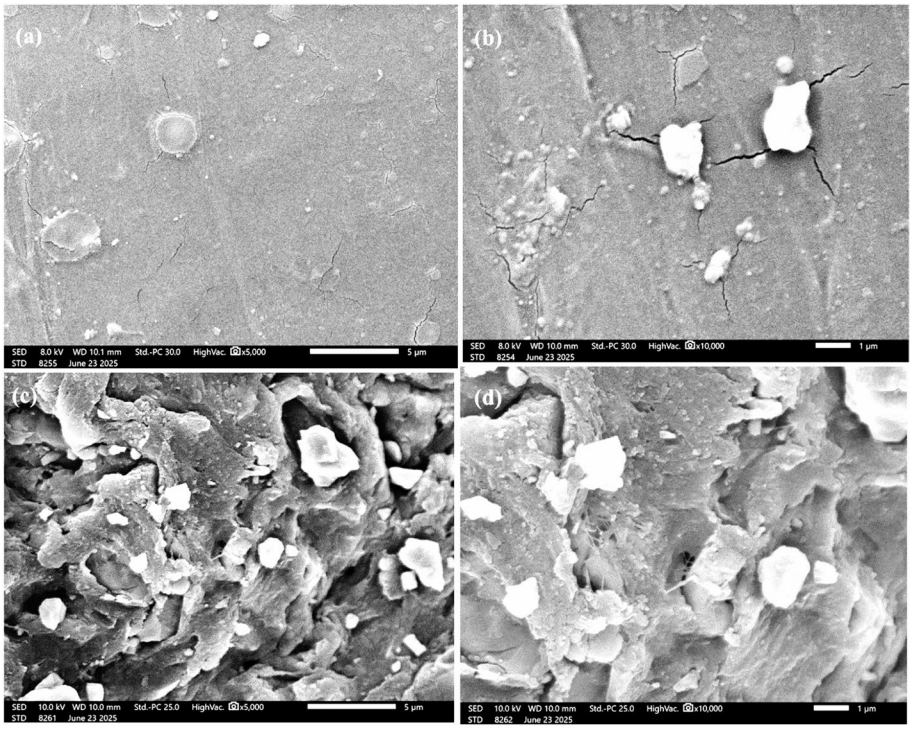

Fig. 6 SEM image of (**a** and **b**) neat LDPE (**c** and **d**) SNB/LDPE composite

ethanol under reflux conditions. During this reaction, the triethoxysilane groups are converted into silanol groups as shown in Eq. 6:

$$\begin{aligned}&(\mathrm{EtO})_3-\mathrm{Si}-(\mathrm{CH_2})_3-\mathrm{NH_2}+3\mathrm{H_2O}\rightarrow\\&(\mathrm{HO})_3-\mathrm{Si}-(\mathrm{CH_2})_3-\mathrm{NH_2}+3\mathrm{EtOH}\end{aligned}\tag{6}$$

The resulting silanol-functionalized silane then undergoes a condensation reaction with the surface hydroxyl groups present on the nano-biochar, forming covalent Si–O–C linkages (Eq. 7):

Table 5 Comparative matrix of flame retardancy performance

Study/reference	Composite system	Additive(s) & loading	LOI (%)	PHRR (kW/m^2)	Residual char (%)	UL-94 rating
This study	PE + SNB + APP	5% SNB + 2% APP	32.5	382.4	17.9	V-0
Mechanical, Thermal, and Fire Retardant Properties of Rice Husk Biochar Reinforced Recycled High-Density Polyethylene Composite Material [9]	Recycled HDPE + Rice Husk Biochar	40% Biochar	25.3	301	Not specified	V-1
Emerging application of biochar as a renewable and superior filler in polymer composites [64].	PP + Biochar	25% Biochar	22.1	Not specified	Not specified	Not specified
Development of Biodegradable Flame-Retardant Bamboo Charcoal Composites, Part I: Thermal and Elemental Analyses [65]	PLA + Bamboo Charcoal + AHP	30% AHP	Not specified	Not specified	Increased RM by 2.39×	Not specified
Talc-Filled HDPE Composites Thermal Stability and Flame Resistance of the Coextruded Wood-Plastic Composites Containing Talc-Filled Plastic Shells [66]	HDPE + Talc	50% Talc	Not specified	323.3	Not specified	Not specified

$$(\mathrm{HO})_3-\mathrm{Si}-(\mathrm{CH_2})_3-\mathrm{NH_2}+\mathrm{Biochar}-\mathrm{OH}\rightarrow \mathrm{Biochar}-\mathrm{O}-\mathrm{Si}-(\mathrm{CH_2})_3-\mathrm{NH_2}+\mathrm{H_2O} \quad (7)$$

This grafting introduces amine-functional alkyl groups onto the carbon surface, significantly improving the compatibility between the polar-modified biochar and the hydrophobic LDPE matrix. As a result, filler dispersion is more uniform, interfacial bonding is stronger, and stress transfer efficiency is enhanced. This accounts for the observed increases in tensile strength and Young's modulus at lower SNB contents. Moreover, the presence of well-dispersed SNB contributes to thermal insulation by increasing phonon scattering and forming a tortuous path that impedes heat flow. The role of SNB becomes even more pronounced when combined with APP, forming a synergistic flame-retardant system. Upon heating, APP undergoes a series of endothermic decomposition reactions, releasing ammonia (NH_3), water (H_2O), and generating phosphoric acid (H_3PO_4), as described in Eq. 8:

$$(\mathrm{NH_4PO_3})\,\mathrm{n}\rightarrow \mathrm{H_3PO_4}+\mathrm{NH_3}+\mathrm{H_2O}+\mathrm{Char} \quad (8)$$

The generated phosphoric acid acts as a dehydrating agent, promoting the formation of a stable, intumescent char layer on the polymer surface. Meanwhile, SNB reinforces this char both physically and thermally by serving as a high-carbon scaffold. The nanobiochar also contributes to the formation of a compact, continuous barrier that slows down heat and mass transfer, enhancing flame resistance. Together, these effects yield a condensed-phase mechanism where the flame-retardant activity is dominated by char formation, barrier protection, and thermal shielding. This mechanism is consistent with previously reported systems combining carbon-based additives with phosphorus-based flame retardants, confirming the synergistic interaction between SNB and APP.

4 Conclusion

This study successfully demonstrated the development and optimization of a multifunctional LDPE composite reinforced with SNB derived from palm kernel shell. Through surface modification using APTES, biochar was effectively functionalized at 2% v/v, as confirmed by FTIR analysis. The modified SNB was incorporated into LDPE at various loadings, with 5 wt% identified as the optimal formulation based on a balance of thermal insulation, mechanical strength, and dispersion quality. At this loading, the composite exhibited a 25% reduction in thermal conductivity, an 18% increase in tensile modulus, and enhanced thermal stability with increased char residue. XRD analysis revealed a slight reduction in crystallinity due to filler-induced disruption of polymer chain packing, while DSC results indicated minimal compromise in thermal transitions. Furthermore, the inclusion of 10 wt% commercial flame retardants APP, $Al(OH)_3$, and $Mg(OH)_2$ into the optimized SNB/LDPE system showed significant improvements in fire resistance, with the SNB/APP composite achieving the best performance. This system reached a LOI of 32.5%, a UL-94 V-0 rating, and a 51% reduction in PHRR, highlighting strong condensed-phase flame retardant synergy. The proposed mechanism, supported by TGA and morphological evidence, attributes these enhancements to the combined effects of APP-induced intumescent char and SNB's thermally stable carbon scaffold. These results underscore the potential of silanized nano-biochar as a sustainable, high-performance additive in thermoplastic composites for applications requiring thermal insulation and fire safety.

5 Limitations of the study

While this study establishes the efficacy of SNB as a multifunctional additive for enhancing thermal insulation and flame retardancy in LDPE composites, several limitations should be noted. First, the investigation was focused on a specific biochar feedstock palm kernel shell and one silane coupling agent (APTES). Although this choice demonstrated excellent performance, the effects of different biomass sources or alternative silanization chemistries were not explored. These factors may influence biochar morphology, reactivity, and compatibility, and could further optimize or diversify composite applications.

Additionally, while key thermal, mechanical, and flame-retardant properties were comprehensively evaluated, long-term stability and weathering resistance under real-world conditions were not assessed in this study. These aspects are crucial for practical deployment in outdoor or high-humidity environments. Furthermore, the dispersion of SNB within the polymer matrix, although improved via silanization, may still be subject to variability at industrial scale, necessitating further rheological and process optimization studies. It should also be noted that the incorporation of additives such as APP, $Al(OH)_3$, and $Mg(OH)_2$ may influence the thermal degradation behavior, crystallinity, mechanical strength, and morphology of the composites. While these effects were not fully characterized here, established literature indicates that moderate changes are expected due to endothermic decomposition, char promotion, and filler–matrix interactions. Therefore, the current study focuses on flame-retardant synergy using an optimized SNB matrix, with comprehensive evaluation of these additional property changes identified as an important direction for future work. Nonetheless, these limitations provide pathways for future research rather than detracting from the current findings, which clearly

demonstrate that 2% APTES-modified SNB at 5 wt% loading offers a scalable, sustainable, and high-performance solution for thermoplastic composite enhancement.

Abbreviations

APTES	3-Aminopropyltriethoxysilane
APP	Ammonium polyphosphate
$Al(OH)_3$	Aluminum hydroxide
BC	Biochar
Cp	Specific heat capacity
DLS	Dynamic light scattering
DSC	Differential scanning calorimetry
FESEM	Field emission scanning electron microscopy
FTIR	Fourier-transform infrared spectroscopy
HDPE	High-density polyethylene
LDPE	Low-density polyethylene
LOI	Limiting Oxygen Index
MCC	Micro combustion calorimetry
$Mg(OH)_2$	magnesium hydroxide
NB	Nano-biochar (unmodified)
PHRR	Peak heat release rate
SEM	Scanning electron microscopy
SNB	Silanized nano-biochar
TGA	Thermogravimetric analysis
Tg	Glass transition temperature
Tm	Melting temperature
Tmax	Temperature at maximum degradation rate
Tonset	Onset degradation temperature
TTI	Time to ignition
UL-94	Underwriters laboratories fire test standard

List of symbols

A	Thermal diffusivity (mm^2/s)
P	Density (g/cm^3)
Cp	Specific heat capacity (J/g·K)
K	Thermal conductivity (W/m·K)
Tg	Glass transition temperature (°C)
Tm	Melting temperature (°C)
Tonset	Onset degradation temperature (°C)
Tmax	Temperature at max degradation rate (°C)
% Char	Residual char content (%)
LOI	Limiting Oxygen Index (%)
PHRR	Peak heat release rate (kW/m^2)
TTI	Time to ignition (s)

Acknowledgements
The authors thank the Tertiary Education Trust Fund (TETFund) for Providing Analytical Equipment to Federal University Wukari.

Author contributions
David Abutu: Conceptualization, Investigation, Data curation, Writing – original draft, Visualisation, Funding acquisition. A. O. Ameh: Writing – review & editing, Supervision. Barima Money & Peter Ujulu: Visualisation, Writing – review & editing. Amani Haruna David: Validation, Writing – review & editing.

Funding
This research received no specific grant from any funding agency in the public, commercial, or non-profit sectors.

Data availability
The datasets generated during and/or analyzed during the current study are available from the corresponding author on reasonable request.

Declarations

Ethics approval and consent to participate
The palm kernel shells used in this study were obtained from *Elaeis guineensis* (oil palm). The material was sourced as an agricultural by-product from the Sri Gambang palm oil processing facility, Malaysia. The collection and use of the palm kernel shells complied with local and national regulations governing the use of plant-derived materials and agricultural waste. The plant material was not collected from wild or protected populations, and no endangered or protected species were involved in this study. Permission to collect and use the palm kernel shells for research purposes was obtained from the management of the Sri Gambang palm oil processing facility. No additional licences were required.

Consent for publication
Not applicable.

Competing interests
The authors declare no competing interests.

Received: 22 January 2026 / Accepted: 23 April 2026
Published online: 27 April 2026

References

1. Zhang D. Fire-Safe Biobased Composites: Enhancing the Applicability of Biocomposites with Improved Fire Performance. Fire. 2023;6(6):229. https://doi.org/10.3390/fire6060229.
2. Xu Y, et al. High-strength, thermal-insulating, fire-safe bio-based organic lightweight aerogel based on 3D network construction of natural tubular fibers. Compos B Eng. 2023;261:110809. https://doi.org/10.1016/j.compositesb.2023.110809.
3. Nguyen TA, Bui TTT, Nguyen TH, Dam XT, Dang HT. Artificial intelligence-assisted design of green-chemically treated banana fiber/epoxy composites for enhanced mechanical and fire-resistant performance. Polym Bull. 2026;83(2):94. https://doi.org/10.1007/s00289-025-06106-6.
4. Temane LT, Ray SS, Orasugh JT. Review on processing, flame-retardant properties, and applications of polyethylene composites with graphene-based nanomaterials. Macromol Mater Eng. 2024. https://doi.org/10.1002/mame.202400104.
5. Lu L et al. Recent advances and applications of flexible phase change composites. EcoMat. 2025. https://doi.org/10.1002/eom2.70004
6. Nguyen TA, Nguyen TH. 2021. Banana fiber-reinforced epoxy composites: mechanical properties and fire retardancy. Int J Chem Engin. 2021: 1–9. https://doi.org/10.1155/2021/1973644
7. Zhang Q, et al. Biochar filled high-density polyethylene composites with excellent properties: Towards maximizing the utilization of agricultural wastes. Ind Crops Prod. 2020;146:112185. https://doi.org/10.1016/j.indcrop.2020.112185.
8. Li M, Park PMNJ, Song J. Functionalization of cotton fibers with a liquid rice husk-derived DOPO hybrid for enhanced flame retardancy and mechanical performance of epoxy composites. Compos Part Appl Sci Manuf. 2026;204:109612. https://doi.org/10.1016/j.compositesa.2026.109612.
9. Shah AR, Imdad A, Sadiq A, Malik RA, Alrobei H, Badruddin IA. Mechanical, thermal, and fire retardant properties of rice husk biochar reinforced recycled high-density polyethylene composite material. Polym (Basel). 2023;15(8):1827. https://doi.org/10.3390/polym15081827
10. Han Y, Mayer D, Offenhäusser A, Ingebrandt S. Surface activation of thin silicon oxides by wet cleaning and silanization. Thin Solid Films. 2006;510:1–2. https://doi.org/10.1016/j.tsf.2005.11.048.
11. Luo Y, et al. A low-density polyethylene composite with phosphorus-nitrogen based flame retardant and multi-walled carbon nanotubes for enhanced electrical conductivity and acceptable flame retardancy. Front Chem Sci Eng. 2021;15(5):1332–45. https://doi.org/10.1007/s11705-021-2035-0.
12. Li M, Park PMNJ, Song J. Enhancing flame-retardant and mechanical properties of epoxy composites through bio-based flame retardant treated cotton fabric reinforcement. Polym Degrad Stab. 2025;232:111109. https://doi.org/10.1016/j.polymdegradstab.2024.111109.
13. Lin Y, Munroe P, Joseph S, Kimber S, Van Zwieten L. Nanoscale organo-mineral reactions of biochars in ferrosol: an investigation using microscopy. Plant Soil. 2012;357:1–2. https://doi.org/10.1007/s11104-012-1169-8.
14. Raczkiewicz M, Mašek O, Ok YS, Oleszczuk P. Size reduction of biochar to nanoscale decrease polycyclic aromatic hydrocarbons (PAHs) and metals content and bioavailability in nanobiochar. Sci Total Environ. 2024;937:173372. https://doi.org/10.1016/j.scitotenv.2024.173372.
15. Li M, Park PMNJ, Song J. Flame-retardant innovations in bio-based treatments for lignocellulosic natural fibers: a review. Int J Biol Macromol. 2025;311:143728. https://doi.org/10.1016/j.ijbiomac.2025.143728.
16. Wang Y, Liu X, Lan T, Yang Q, Cong S, Lin Y. Corn stalk biochar-reinforced high-density polyethylene material: flame-retardant and anti-aging properties. Fibers Polym. 2023;24(5):1771–9. https://doi.org/10.1007/s12221-023-00044-8.
17. Das O, Kim NK, Kalamkarov AL, Sarmah AK, Bhattacharyya D. Biochar to the rescue: Balancing the fire performance and mechanical properties of polypropylene composites. Polym Degrad Stab. 2017;144:485–96. https://doi.org/10.1016/j.polymdegradstab.2017.09.006.
18. Ma Z, et al. Evolution of the chemical composition, functional group, pore structure and crystallographic structure of biochar from palm kernel shell pyrolysis under different temperatures. J Anal Appl Pyrol. 2017;127:350–9. https://doi.org/10.1016/j.jaap.2017.07.015.
19. Nusrat Aman AM, Selvarajoo A, Lau TL, Chen W-H. Optimization via response surface methodology of palm kernel shell biochar for supplementary cementitious replacement. Chemosphere. 2023;313:137477. https://doi.org/10.1016/j.chemosphere.2022.137477.
20. Nyah F et al. Bibliometric insights into cellulose nanoparticles: advancing sustainable enhanced oil recovery in HTHP reservoirs. In: SPE Nigeria annual international conference and exhibition, SPE. 2025. https://doi.org/10.2118/228643-MS
21. Raczkiewicz M, Ostolska I, Mašek O, Oleszczuk P. Effect of the pyrolysis conditions and type of feedstock on nanobiochars obtained as a result of ball milling. J Clean Prod. 2024;458:142456. https://doi.org/10.1016/j.jclepro.2024.142456.
22. Naghdi M, et al. A green method for production of nanobiochar by ball milling- optimization and characterization. J Clean Prod. 2017;164:1394–405. https://doi.org/10.1016/j.jclepro.2017.07.084.
23. Song B, Chen M, Zhao L, Qiu H, Cao X. Physicochemical property and colloidal stability of micron- and nano-particle biochar derived from a variety of feedstock sources. Sci Total Environ. 2019;661:685–95. https://doi.org/10.1016/j.scitotenv.2019.01.193.
24. Zhang Y, Fei D, Xin G, Cho U-R. Surface modification of novel rice bran carbon functionalized with (3-Mercaptopropyl) trimethoxysilane and its influence on the properties of styrene-butadiene rubber composites. J Compos Mater. 2016. 50(21): 2987–2999. https://doi.org/10.1177/0021998315615202
25. Nguyen TA, Nguyen QT. Hybrid biocomposites based on used coffee grounds and epoxy resin: mechanical properties and fire resistance. Int J Chem Engin. 2021. https://doi.org/10.1155/2021/1919344
26. Nguyen TA, Nguyen TH. Study on mechanical properties of banana fiber-reinforced materials poly (Lactic Acid) composites. Int J Chem Eng. 2022. https://doi.org/10.1155/2022/8485038.

27. Abdo HS, Alnaser IA, Seikh AH, Mohammed JA, Ragab SA, Fouly A. Ecofriendly Biochar as a Low-Cost Solid Lubricating Filler for LDPE Sustainable Biocomposites: Thermal, Mechanical, and Tribological Characterization. Int J Polym Sci. 2023;2023:1–13. https://doi.org/10.1155/2023/2445472.
28. Vidakis N, et al. Reinforced HDPE with optimized biochar content for material extrusion additive manufacturing: morphological, rheological, electrical, and thermomechanical insights. Biochar. 2024;6(1):37. https://doi.org/10.1007/s42773-024-00314-5.
29. Yerima EA, et al. Efficient and optimal adsorptive removal of urea from agricultural effluent using acidified ball clay: optimization via response surface methodology. Afr Sci Rep. 2026;367. https://doi.org/10.46481/asr.2026.5.1.367.
30. Yerima EA, et al. An efficient and optimal adsorptive removal of glufosinate ammonium from wastewater using carbonized rice husk-clay blend briquettes. Ecol Eng Environ Technol. 2025;26(9):1–12. https://doi.org/10.12912/27197050/208147.
31. Nyah F, et al. Cellulose bionanomaterial design for enhanced oil recovery: A review of existing, emerging technologies and future outlook. Petroleum Res. 2025. https://doi.org/10.1016/j.ptlrs.2025.12.002.
32. Money B, et al. Characterization of Kuala Rompin clay (KRC) and empty fruit bunch ash (EFBA) for potential application in the formulation of geopolymer cement. Discover Concrete Cem. 2025. https://doi.org/10.1007/s44416-025-00012-w.
33. Money B, et al. A review on advancing clay-based geopolymers for high-temperature oil well cements: Mechanisms, durability, and applications. Petroleum Res. 2025. https://doi.org/10.1016/j.ptlrs.2025.08.005.
34. Nguyen TA, et al. Enhancing epoxy composite materials through lime-treated sugarcane bagasse and glass fiber reinforcement: Morphological, mechanical, and flame-retardant insights. Vietnam J Chem. 2025;63(1):68–80. https://doi.org/10.1002/vjch.202400059.
35. Ameh AO, Abutu D, Andoor S. Effect of Process Parameters on the Viscosity and pH of Acetic Anhydride Modified Cassava Starch. Nigerian J Pharm Appl Sci Res. 2020;7(1):22–8.
36. Abutu D et al. Optimization of ethanol fermentation in a bubble column bioreactor using response surface methodology with ferric oxide nanoparticle-modified supports. In: SPE Nigeria annual international conference and exhibition, SPE. 2025. https://doi.org/10.2118/228638-MS
37. Qiu M et al. Biochar for the removal of contaminants from soil and water: a review. Biochar. 2022. https://doi.org/10.1007/s42773-022-00146-1
38. Abutu D, Aderemi BO, Ameh AO, Yussof HW, Agi A. Nano-enhanced biocarriers: ferric oxide-modified chitosan and calcium alginate beads for improved fermentation efficiency and reusability in a bubble column bioreactor. Biotechnol Lett. 2025;47(4):70. https://doi.org/10.1007/s10529-025-03611-6.
39. Liu Y, He Z, Uchimiya M. Comparison of biochar formation from various agricultural by-products using FTIR spectroscopy. Mod Appl Sci. 2015. https://doi.org/10.5539/mas.v9n4p246.
40. Gęca M, et al. Surface Treatment of Biochar—Methods, Surface Analysis and Potential Applications: A Comprehensive Review. Surfaces. 2023;6(2):179–213. https://doi.org/10.3390/surfaces6020013.
41. Nanda S, Mohanty P, Pant KK, Naik S, Kozinski JA, Dalai AK. Characterization of North American Lignocellulosic Biomass and Biochars in Terms of their Candidacy for Alternate Renewable Fuels. Bioenergy Res. 2013;6(2):663–77. https://doi.org/10.1007/s12155-012-9281-4.
42. Dhali K, Daver F, Cass P, Adhikari B. Surface modification of the cellulose nanocrystals through vinyl silane grafting. Int J Biol Macromol. 2022;200:397–408. https://doi.org/10.1016/j.ijbiomac.2022.01.079.
43. Lee JH, Kim SH. Fabrication of silane-grafted graphene oxide and its effect on the structural, thermal, mechanical, and hysteretic behavior of polyurethane. Sci Rep. 2020;10(1):19152. https://doi.org/10.1038/s41598-020-76153-8.
44. Chiu W-M, Kuo H-Y, Tsai P-A, Wu J-H. Preparation and Properties of Poly (Lactic Acid) Nanocomposites Filled with Functionalized Single-Walled Carbon Nanotubes. J Polym Environ. 2013;21(2):350–8. https://doi.org/10.1007/s10924-012-0514-6.
45. Lucia A, Bacher M, van Herwijnen HWG, Rosenau T. A Direct Silanization Protocol for Dialdehyde Cellulose. Molecules. 2020;25(10):2458. https://doi.org/10.3390/molecules25102458.
46. Magee E, Tang F, Walker M, Zak A, Tenne R, McNally T. Silane functionalization of WS_2 nanotubes for interaction with poly(lactic acid). Nanoscale. 2023a;15(16):7577–90. https://doi.org/10.1039/D3NR00583F.
47. Nnadozie EC, Ajibade PA. Adsorption, kinetic and mechanistic studies of Pb(II) and Cr(VI) ions using APTES functionalized magnetic biochar. Microporous Mesoporous Mater. 2020;309:110573. https://doi.org/10.1016/j.micromeso.2020.110573.
48. Coombs SG, Khodjaniyazova S, Bright FV. Exploiting the 3-Aminopropyltriethoxysilane (APTES) autocatalytic nature to create bioconjugated microarrays on hydrogen-passivated porous silicon. Talanta. 2018;177:26–33. https://doi.org/10.1016/j.talanta.2017.09.038.
49. Abutu D, Aderemi BO, Ameh AO, Wan Yussof H, Yerima EA, Agi A. Integrated experimental and numerical study of a bubble column bioreactor with immobilized S. cerevisiae for ethanol production in non-Newtonian fermentation broth. Chem Eng Commun. 2025. https://doi.org/10.1080/00986445.2025.2572738.
50. Nyah F, et al. Cellulose Bionanomaterial Design for Enhanced Oil Recovery: A Review of Existing, Emerging Technologies and Future Outlook. Petroleum Res. 2025. https://doi.org/10.1016/j.ptlrs.2025.12.002.
51. Abutu D, et al. Reinforcing concrete with nano-enhanced bio-additives: a path toward sustainable construction materials. Discover Concrete Cem. 2025;1(1):20. https://doi.org/10.1007/s44416-025-00022-8.
52. Michailidis N, et al. Printability and thermomechanical metrics of high-density polyethylene doped with nano antimony TiN oxide. Eur J Mater. 2025. https://doi.org/10.1080/26889277.2025.2463330.
53. Zaki N. S., Salih T. W. The effect of crystallinity on the thermal conductivity of polymers. J Eng Sustain Dev. 2021;25:2–25. https://doi.org/10.31272/jeasd.conf.2.2.4.
54. Yu Y, et al. A Low-Density Polyethylene-Reinforced Ternary Phase-Change Composite with High Thermal Conductivity for Battery Thermal Management. Energies (Basel). 2023;16(9):3838. https://doi.org/10.3390/en16093838.
55. Yousefi Y, Tariku F. Thermal conductivity and specific heat capacity of insulation materials at different mean temperatures. J Phys Conf Ser. 2021. 2069(1): 012090. https://doi.org/10.1088/1742-6596/2069/1/012090
56. Tsou C-H, et al. Enhanced performance of nanoplate-carbon nanotube reinforced poly(butylene succinate) nanocomposites for sustainable packaging and multifunctional applications. Food Chem X. 2025;31:102989. https://doi.org/10.1016/j.fochx.2025.102989.
57. Rezvani Ghomi E, et al. The Flame Retardancy of Polyethylene Composites: From Fundamental Concepts to Nanocomposites. Molecules. 2020;25:5157. https://doi.org/10.3390/molecules25215157.

58. Shen L, Li J, Li R, Lin H, Chen J, Liao B-Q. A new strategy to produce low-density polyethylene (LDPE)-based composites simultaneously with high flame retardancy and high mechanical properties. Appl Surf Sci. 2018;437:75–81. https://doi.org/10.1016/j.apsusc.2017.12.149.
59. Feng C, Liang M, Jiang J, Huang J, Liu H. Flame retardancy and thermal degradation behavior of efficient intumescent flame retardant LDPE composite containing 4A zeotile. J Anal Appl Pyrol. 2016;118:9–19. https://doi.org/10.1016/j.jaap.2015.12.008.
60. Nie S, et al. Thermal and flame retardant properties of novel intumescent flame retardant low-density polyethylene (LDPE) composites. J Therm Anal Calorim. 2012;109(2):999–1004. https://doi.org/10.1007/s10973-011-1819-8.
61. Ou H, Ran Y, Pan M, Xue H. Study on the effect of novel intumescent flame retardant composed of β-cyclodextrin modified ammonium polyphosphate and THEIC on the flame retardancy of LDPE composites. J Loss Prev Process Ind. 2024;87:105211. https://doi.org/10.1016/j.jlp.2023.105211.
62. Qin R, Zhang X, Kong F, Yang J, Nie S. Investigation on novel flame retardant low-density polyethylene composites based on THEIC and MCAPP. J Polym Res. 2019;26(6):144. https://doi.org/10.1007/s10965-019-1810-9.
63. Wang NN, Xiang DH, Mo PS, Lu Y. Flame retardant low density polyethylene with aluminium hydroxide/commercial fire retardants fr01 synergistic system. Adv Mat Res. 2013. https://doi.org/10.4028/www.scientific.net/AMR.652-654.485.
64. Tengku Yasim-Anuar TA, et al. Emerging application of biochar as a renewable and superior filler in polymer composites. RSC Adv. 2022;12(22):13938–49. https://doi.org/10.1039/D2RA01897G.
65. Wang S, Zhang L, Semple K, Zhang M, Zhang W, Dai C. Development of Biodegradable Flame-Retardant Bamboo Charcoal Composites, Part I: Thermal and Elemental Analyses. Polym (Basel). 2020;12(10):2217. https://doi.org/10.3390/polym12102217.
66. Huang R, Zhang X, Chen Z, Wan M, Wu Q. Thermal Stability and Flame Resistance of the Coextruded Wood-Plastic Composites Containing Talc-Filled Plastic Shells. Int J Polym Sci. 2020;2020:1–9. https://doi.org/10.1155/2020/1435249.

Publisher's Note

Springer Nature remains neutral with regard to jurisdictional claims in published maps and institutional affiliations.